Kobe University Repository : Kernel

PDF issue: 2026-11-09

Sub-Bandgap Photocurrent Enhancement in Silicon Nanodisk Hexagonal Array Induced by Fabry-Pérot Bound States in the Continuum

Moriasa, Keisuke
Hasebe, Hiroaki
Sugimoto, Hiroshi
Fujii, Minoru

(Citation)
ACS Photonics,12(3):1658-1665

(Issue Date)
2025-03-19

(Resource Type)
journal article

(Version)
Accepted Manuscript

(Rights)
This document is the Accepted Manuscript version of a Published Work that appeared in final form in ACS Photonics, copyright © 2025 American Chemical Society after peer review and technical editing by the publisher. To access the final edited and published work see https://doi.org/10.1021/acsphotonics.4c02596

(URL)
https://hdl.handle.net/20.500.14094/0100493608

KOBE UNIVERSITY

Sub-bandgap Photocurrent Enhancement in Silicon Nanodisk Hexagonal Array Induced by Fabry-Pérot Bound States in the Continuum

Keisuke Moriasa, Hiroaki Hasebe, Hiroshi Sugimoto*, and Minoru Fujii*

Department of Electrical and Electronic Engineering, Graduate School of Engineering, Kobe University, Rokkodai, Nada, Kobe 657-8501, Japan

Abstract

We develop a silicon (Si) nanodisk array on a gold (Au) mirror structure as a platform for a Si-based narrow band photodetector operating in the sub-bandgap wavelength range. Numerical simulations reveal that the structure possesses the Fabry-Pérot bound states in the continuum (BIC) arising from the destructive interference between the toroidal dipole (TD) resonance of the nanodisk array and the mirror dipole. At the critical coupling conditions, narrow band perfect absorption is achieved even if the extinction coefficient of Si nanodisks is very small. We produce the designed structure by a nanosphere lithography and studied the reflectance and photocurrent spectra as a function of the distance between a Si nanodisk array and a Au mirror. We demonstrated that the photocurrent can be enhanced in the sub-bandgap wavelength range at the critical coupling condition, and the enhancement factor is modulated by the Si nanodisk array - mirror distance.

Keywords: toroidal dipole, Mie resonance, photodetector, dielectric nanodisk, perfect absorption

Introduction

Near infrared (NIR) radiation beyond 1400 nm in wavelength has high eye safety and minimum propagation loss in fog, and is suitable for free space optical telecommunication and LiDARs.[1] Photodetectors used in that wavelength range are photodiodes of narrow band gap semiconductors such as Ge, InGaAs, and InSb. As a low-cost and CMOS compatible alternative of these devices, several new types of silicon (Si)-based photodetectors operating beyond 1400 nm have been proposed.[2,3] A well-studied device is a Schottky junction between Si and metal

nanostructures having the localized surface plasmon resonances (LSPRs) in the NIR range.[4–7] NIR radiation excites LSPRs of metal nanostructures, which decay into hot electrons having the energy large enough to overcome the Schottky barrier and generate photocurrent.[8] Another widely studied approach to extend the operation wavelength range of Si-based photodetectors is utilizing the defect mediated sub-bandgap absorption of poly-crystalline Si.[9–12] In order to increase sub-bandgap absorption of poly-crystalline Si,[13,14] defect states are actively controlled by impurity doping.[11,12,15,16] For example, defect formation by high concentration (10^{17}-10^{20} cm^{-3}) Ar doping strongly enhances the absorption at 1.31 μm, and a photodetector with the detectivity of 10^{11} $cmHz^{1/2}/W$ is reported.[12]

The defect-engineering approach can be combined with optical resonances to further enhance the detectivity and to achieve narrow-band photodetection.[9,10,17–19] Different types of optical resonators have been proposed for the enhancement of Si sub-bandgap absorption. For example, a micrometer size Si sphere with the whispering gallery mode enhances the photoresponsivity around 1500 nm.[19] In a Si photodetector using waveguide modes, responsivity of 0.8 A/W is achieved at 1550 nm.[9] In previous work, we demonstrated that toroidal dipole (TD) resonances in a thin Si nanodisk hexagonal array enhance the sub-bandgap absorption and the photoresponsivity in a narrow spectral range.[20] Furthermore, numerical simulations indicated that the TD resonances can induce bound states in the continuum (BICs) via coupling with a Fabry Pérot cavity and perfect absorption is achieved in a very small extinction coefficient wavelength range.[21]

In this work, we implement the Fabry-Pérot BIC induced by the TD resonance to a real device and demonstrate the applicability for narrow band photocurrent enhancement in a Si sub-bandgap wavelength range. The device is composed of a hexagonal array of Si nanodisks having the TD resonance and a gold (Au) mirror separated by a silicon dioxide (SiO_2) spacer. First, we perform numerical simulations to clarify structural parameters and conditions to achieve perfect absorption in a wide extinction coefficient range (10^{-4}-10^{-2}) and discuss the condition to maximize absorptance in the Si region for the photocurrent enhancement. We then fabricate the designed structure with a varying SiO_2 spacer thickness, and study the reflectance and photocurrent spectra as a function of the spacer thickness.

Results and Discussion

Figure 1(a) shows schematic illustration of the structure studied in this work. A Si thin film with a hexagonal array of thin Si nanodisks on the surface is formed on a Au mirror via a SiO_2 spacer. Figure 1(b) shows the calculated reflectance, transmittance, and absorptance spectra

under normal incidence from the nanodisk side for the structure without a Au mirror. The period (*P*), diameter (*D)*, and height (*H*) of the Si nanodisks are 750 nm, 700 nm, and 100 nm, respectively. The thickness of the Si thin film (*T*) is 40 nm. The refractive index of Si is fixed to 3.5 because of the small dispersion in the sub-bandgap range.[14] The extinction coefficient (κ_{Si}) is assumed to be 10^{-3}. We will study the effect of the extinction coefficient on the spectra later. Despite the very small extinction coefficient, a clear absorption peak is observed at 1480.3 nm, although the peak absorptance is relatively small (0.13). Figure 1(c) shows the plan- and cross-sectional views of the electric field distribution at 1480.3 nm. The field distributions confirm excitation of a TD resonance and strong electric field confinement in the Si region.[22,23] Note that the TD resonance wavelength can be controlled in a wide wavelength range by the structural parameters (*D, H, T*, etc.).[20,23]

From the temporal coupled mode theory (TCMT), the absorptance of a *N*-port resonant system under excitation through port 1 is described as,

$$A = \frac{2\gamma_1 \Gamma_{abs}}{(\omega - \omega_0)^2 + (\Gamma_{rad} + \Gamma_{abs})^2}, \qquad \Gamma_{rad} = \sum_{j=1}^{N} \frac{\gamma_j}{2}, \tag{1}$$

where $\sqrt{\gamma_j}$ is the coupling strength between the resonant cavity and far field radiation via a *j*-th radiating port, Γ_{abs} and Γ_{rad} are the absorption and radiation loss rates of the cavity, respectively.[24–27] In the structure in Figure 1(b), we have two ports ($N = 2$). In this case, the maximum absorptance at the critical coupling condition ($\Gamma_{rad} = \Gamma_{abs} = \Gamma$) is $\gamma_1/2\Gamma$, and the value is smaller than 50%. On the other hand, if the second port is closed, the absorptance can reach 100% at the critical coupling condition. The second port can be closed by placing a mirror below the metasurface as schematically shown in the inset in Figure 1(d). In this configuration, the TD resonance in each nanodisk interferes with its image dipole in the Au mirror as schematically shown in the right image in Figure 1(a). The interference suppresses or promotes the radiation loss rate of the TD resonance (Γ_{rad}) following the $\Gamma_{rad} = \Gamma_0(1 - \cos\psi)$ relation, where Γ_0 is the radiation loss rate of the TD resonance without the mirror and ψ is the propagating phase shift (Note 1 in Supporting Information for details in TCMT).[28,29] When the radiation loss is perfectly suppressed, the toroidal mode turns into a BIC. This is the Fabry Pérot BIC, and is conceptually different from TD-based symmetry protected BICs reported previously.[30,31] In the structure in Figure 1(d), ψ, and concequently Γ_{rad}, can be controlled by the SiO_2 spacer thickness. The independent control of Γ_{rad} without affecting the resonance wavelength of the TD is an advantage of the Fabry Pérot BICs. Figure 1(f) shows the contour plot of the absorptance spectra for different spacer thicknesses. The narrow absorptance peak

around 1480 nm is the TD resonance and the broad bands appearing around S = 450 nm and 950 nm are the Fabry-Pérot modes (Figure S2 in Supporting Information for the electric field distribution). The peak absorptance and linewidth of the TD resonance depend on the spacer thickness, and at S = 340 nm and 840 nm, the peak disappears. These are the Fabry-Perot BICs,[21,29,32–34] where the incident light doesn't interact with the TD mode and is reflected by the Au mirror. By slightly detuning the spacer thickness from the BIC conditions, the absorptance peaks reappear. At the critical coupling conditions (S = 400, 700, 920, and 1200 nm), the absorptance becomes maximum. Figure 1(d) shows the reflectance and absorptance spectra for S = 700 nm. The peak absorptance reaches >0.99 and the quality factor (Q-factor) of the resonance is 880. The electric field distribution in the Figure 1(e) indicates that the field is concentrated in the Si region. The maximum field enhancement factor in the Si region is 2.8 times larger than that of the structure without the mirror (Figure 1(c)).

In Figure 1(a-f), the extinction coefficient of Si is assumed to be 10^{-3}. Since the extinction coefficient of amorphous or polycrystalline Si in the sub-bandgap wavelength range strongly depends on the deposition process and the parameters,[14,35–38] we calculated the absorption spectra for different extinction coefficient values. Figure 1(g) shows the results for $\kappa_{Si} = 10^{-2}$. The overall feature is similar to that of Figure 1(f). For example, the spacer thicknesses satisfying the BIC conditions (indicated by circles) are almost independent of κ_{Si}. On the other hand, the absorption bands are broadened, and the spacer thicknesses satisfying the critical coupling conditions (indicated by horizontal arrows) are significantly changed.

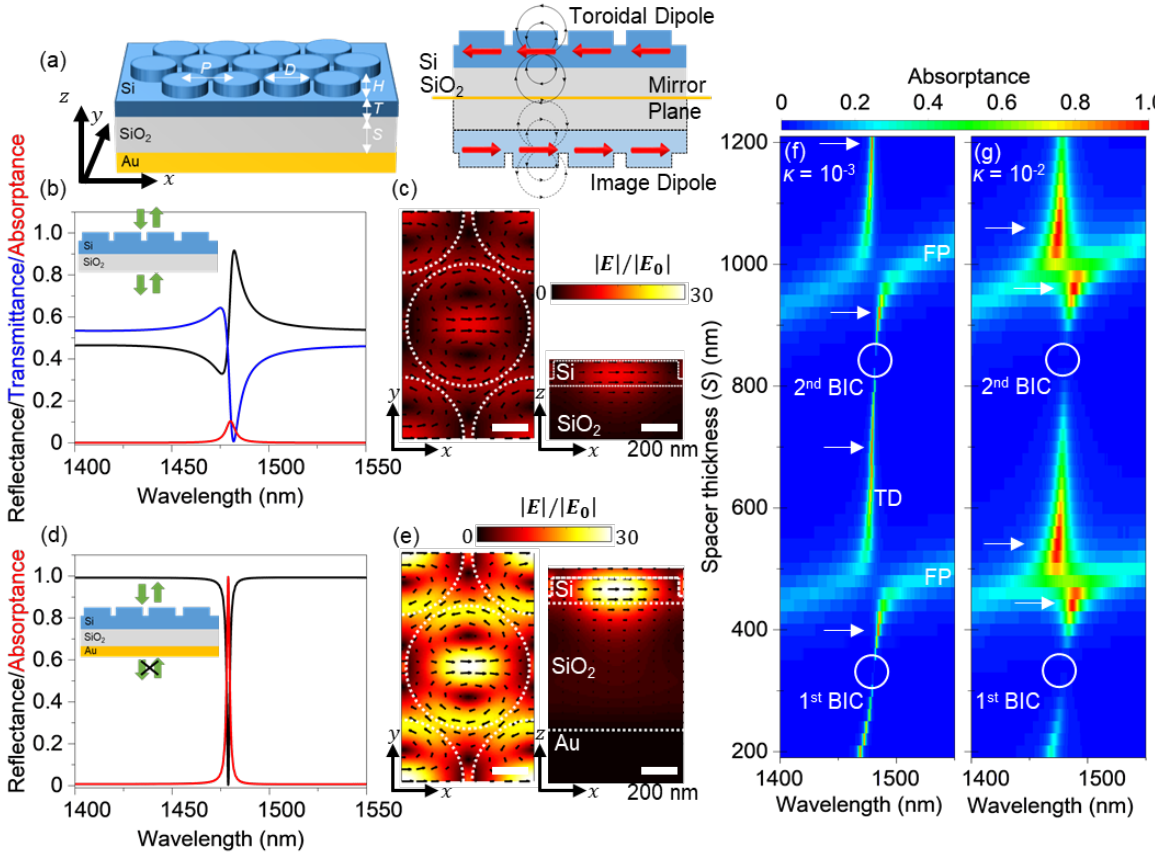


Figure 1. (a) (Left) Schematic of a Si nanodisk array on a Au mirror structure. Definition of the structural parameters are shown. (Right) Illustration representing the concept of interference between TDs in a Si nanodisk array and their image dipoles in a Au mirror. (b) Reflectance (black), transmittance (blue), and absorptance (red) spectra of a Si nanodisk hexagonal array in case without a bottom mirror (P = 750 nm, D = 700 nm, H = 100 nm, and T = 40 nm). (c) Electric field distribution of the structure in (b) at the absorption peak wavelength (1480.3 nm) in x-y (left) and x-z (right) planes. Black arrows are the electric field vectors, and white dashed lines are the outline of the structure. (d) Reflectance (black) and absorptance (red) spectra of a Si nanodisk hexagonal array on a Au mirror structure (P = 750 nm, D = 700 nm, H = 100 nm, T = 40 nm, and S = 700 nm). (e) Electric field distribution of the structure in (d) at the absorption peak wavelength (1479.8 nm) in x-y (left) and x-z (right) planes. (f, g) Contour plots of absorptance spectra of a Si nanodisk array on a Au mirror structure (P = 750 nm, D = 700 nm, H = 100 nm, and T = 40 nm). The spacer thickness (S) is changed from 200 to 1200 nm. The refractive index is 3.5, and the extinction coefficient is (f) 10^{-3} and (g) 10^{-2}. Fabry-Pérot BICs are designated by white circles, and the critical coupling conditions are designated by white arrows.

In Figure 2(a-c), the relation between the κ_{Si} value and the peak absorptance is shown for different spacer thicknesses. The extinction coefficient is changed from 10^{-4} to 10^{-1}. Figure 2(a) shows the data for S = 800 nm. The peak absorptance depends strongly on κ_{Si} and is the largest at very small κ_{Si} (10^{-4}). This is because the radiation loss rate is very small at S = 800 nm, and thus the critical coupling condition is satisfied at very small κ_{Si}. In the figure, in addition to the total absorptance (black), those of Si (red) and Au (blue) are separately shown. Although the total absorptance is 100 %, that in Si is ~60 % and the rest is absorbed in Au. Therefore, at most, only 60 % of absorbed photons contribute to the photocurrent even under the critical coupling condition.

If the radiation loss rate is increased by further detuning the spacer thickness from the BIC condition, the extinction coefficient satisfying the critical coupling condition increases. Figure 2(b) shows the results for S = 700 nm. In this case, the critical coupling condition is satisfied at κ_{Si} = 10^{-3}, and 90 % of incident photons are absorbed by Si. Further decrease of S to 540 nm increases the optimum κ_{Si} to 10^{-2} (Figure 2(c)). In this situation, incident photons are almost solely absorbed by the Si layer. Note that, at high κ_{Si}, absorptance by the Fabry Pérot modes becomes nonnegligible. Figure 2(d) shows absorptance by a Fabry Pérot mode (1380 nm for S = 910 nm) as a function of κ_{Si}. The absorptance starts to increase above κ_{Si} = ~10^{-2}.

Figure 2(e) shows the absorptance in Si and Au at the critical coupling conditions as a function of κ_{Si}. In the top panel, spacer thicknesses satisfying the critical coupling conditions in S =500 – 1000 nm range are shown, and in the middle panel, the Q-factor is shown. The bottom panel is the absorptance in Si and Au. We can see the trade-off between the absorptance in Si and the Q-factor. If a high Q-factor is not required, a relatively large κ_{Si} (e.g., 10^{-2}) is optimum for maximizing the photocurrent in a Si nanodisk layer. On the other hand, if a very high Q-factor is required, the photocurrent enhancement factor is partially sacrificed because of the absorption by Au. The increase of Au absorption at smaller κ_{Si} is due to increased light transmittance in the Si layer. This trade-off can be avoided if we adopt a loss-less Bragg reflector instead of the Au mirror. In Supporting Information (Figure S3), we show simulation results for a Si nanodisk array on a Si/SiO_2 Bragg reflector. Absorptance of the top Si nanodisk layer reaches over 98 % at κ_{Si}= 10^{-3}.

In Figure 2, we focused on critical coupling conditions near the 2nd BIC. We performed similar calculations for critical coupling conditions near the 1st BIC condition, i.e., S ≤ 400 nm. The results are shown in Supporting Information (Figure S4). Near the 1st BIC condition, especially below the 1st BIC condition (S < 340 nm), Au absorption becomes very large. Therefore, critical coupling conditions near the 2nd BIC is more preferable for the photocurrent enhancement.

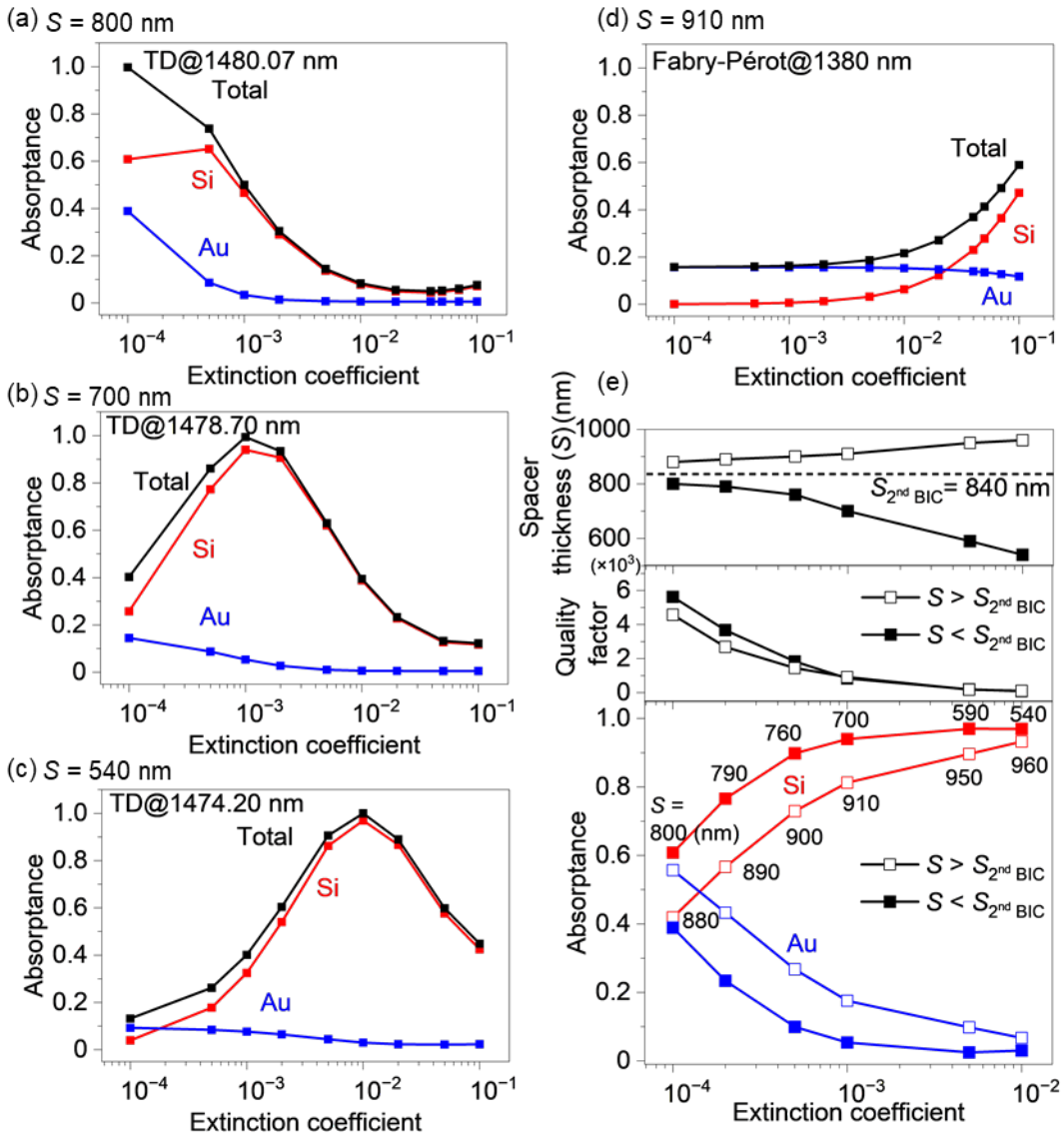


Figure 2 (a-c) Absorptance (black) as a function of $\boldsymbol{\kappa_{Si}}$ at the TD resonance wavelengths for different S; (a) S = 800 nm, (b) S = 700 nm, and (c) S = 540 nm. The other structural parameters are fixed (P = 750 nm, D = 700 nm, H = 100 nm, and T = 40 nm). Absorptances in Si (red) and Au (blue) regions are also shown. (d) Total absorptance and absorptance in Si (red) and Au (blue) regions due to the Fabry Pérot resonance at 1380 nm for S = 910 nm as a function of $\boldsymbol{\kappa_{Si}}$. (e) (Top) Spacer thickness satisfying the critical coupling conditions in S = 500 - 1000 nm range as a function of $\boldsymbol{\kappa_{Si}}$. (Middle) Quality factor of the TD resonance. (Bottom) Absorptance in Si (red) and Au (blue) regions at the critical coupling conditions. The open squares (□) represent the critical coupling conditions above the BIC condition (S =

840 nm), while the closed squares (■) represent those below the BIC condition. The spacer thicknesses are shown in the figure.

Fabrication of Si nanodisk array on mirror structure and the photocurrent spectrum

Figure 3(a) shows the procedure for the fabrication of a Si nanodisk array on a mirror structure. A Au thin film (100 nm in thickness) with thin titanium (Ti) adhesion layers (5 nm in thickness) on both sides was deposited on a SiO_2 substrate 1.3 × 2.5 cm in size by vacuum evaporation (SVC-700T, Sanyu Electron). Then, a SiO_2 spacer layer with the thickness gradient (700 – 1200 nm) along the longer direction of the substrate was deposited by RF magnetron sputtering (SPF-210H, ANELVA) by intentionally offsetting the substrate from the center.[39] On the SiO_2 spacer, an a-Si film 140 nm in thickness was deposited by the same sputtering apparatus. On the a-Si film, a Si nanodisk array was fabricated by the following procedure.[20,23] A hexagonal array of polystyrene (PS) beads (750 nm in diameter) was formed at air/water interface and was transferred onto the a-Si film. The PS beads were then etched by oxygen plasma (L-201D, ANELVA) until the diameter is reduced to ~700 nm. The a-Si film was then etched by Ar^+ ion milling by using the PS bead hexagonal array as an etching mask until the disk height becomes ~100 nm, i.e., the thickness of the remaining film is ~40 nm (atomic force microscopy (AFM) image in Figure S5 in Supporting Information). Finally, the PS beads were removed by Toluene. Figure 3(b) and (c) show the plan- and cross-sectional scanning electron microscope (SEM) images, respectively, of the nanodisk array. Finally, aluminum (Al) electrodes were deposited for the photocurrent measurements as schematically shown in the plan view illustration in Figure 3(a). The distance between the electrodes is 300 μm.

Figure 3(d) shows the reflectance measurement setup. A custom-built inverted optical microscope was used. The metasurface was illuminated from the normal to the surface by a Köhler illumination system with a 10-fold objective lens (N.A. = 0.3). The reflected light is collected by the same objective lens and transferred to the monochromator (Kymera 328i, Andor) and detected by a cooled InGaAs diode array (iDus, Andor). The detected area is 20× 50 μm^2. Reflectance spectra are measured every 700 μm along the longer direction, i.e., the direction of the spacer thickness gradient, of a sample. Figure 3(e) shows the photocurrent measurement setup. The metasurface was illuminated by a supercontinuum laser (SuperK EVO, NKT Photonics) monochronized by an acousto-optic tunable filter (AOTF) (SuperK SELECT IR, NKT Photonics) through a 2-fold objective lens (N.A. = 0.055). The diameter of the laser spot is about 150 μm (Figure S6 in Supporting Information). Photocurrent was measured by a

lock-in amplifier (SR830, Stanford Research System). The bias voltage was 0.2 V (Keithley 236). Note that within the width of an electrode, the spacer thickness changes slightly because of the gradient of the thickness. However, the thickness change from one side of an electrode to the other side is about 5 nm, and it does not affect the optical response significantly.

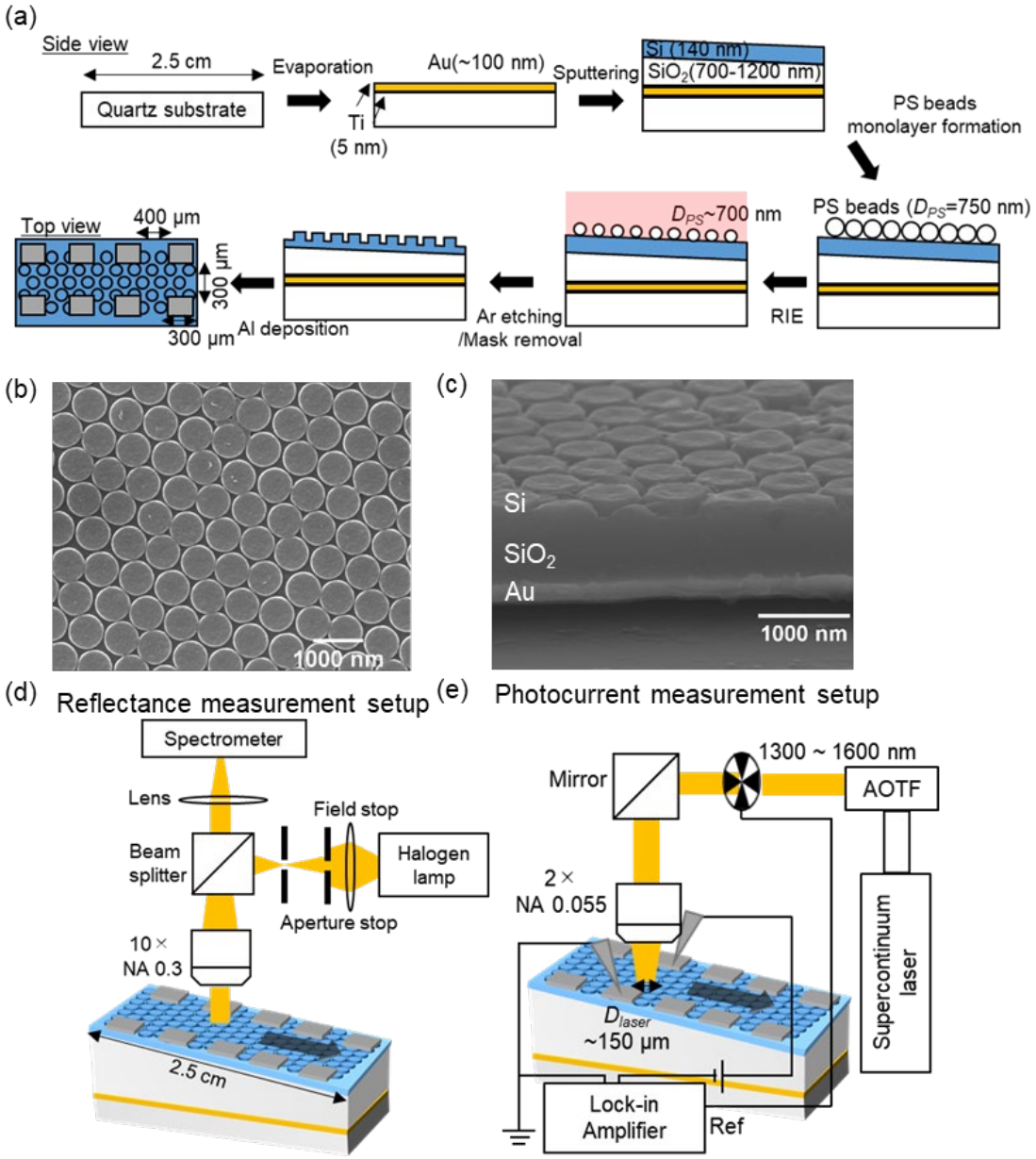


Figure 3. (a) Schematic of the fabrication procedure of a Si nanodisk array on a Au mirror structure. The SiO_2 spacer has a thickness gradient along the long side of a sample. (b) Plan and (c) cross-sectional SEM images of a fabricated structure. (d) Reflectance spectrum measurement setup. (e) Photocurrent spectrum measurement setup. Reflectance and photocurrent spectra are measured every 700 μm along the long side of the substrate by

moving a sample stage, and thus the spacer thickness dependences are measured in one sample.

Figure 4 (a) and (b) shows the contour plot of measured and calculated (n = 3.5 and κ_{Si} = 4 $\times 10^{-2}$) reflectance spectra. The spacer thickness is changed from 700 to 1200 nm. The measured and calculated spectra show overall agreement. The reflectance dips indicated by white dashed lines are the Fabry Pérot resonances. The spacer thickness independent dip around 1450 nm is the TD resonance, while that around 1040 nm is the MD resonance (see the electric field distribution at 1040 nm in Figure S8 in Supporting Information). At $S \approx$ 770 and 1175 nm, the reflectance dip almost disappears. These are the Fabry-Pérot BICs. On the other hand, at S = 923 nm, the reflectance decreases to 0.05 at 1434 nm, suggesting that the critical coupling condition is almost satisfied.

Figure 4(c) (black squares) shows the Q-factor of the reflectance dip obtained by fitting the experimental reflectance spectra with a Lorentz function as a function of S. The Q-factors obtained from the calculated reflectance spectra for three different extinction coefficients (κ_{Si} = 1×10^{-3}, 1×10^{-2}, 4×10^{-2}) are also shown. The experimentally obtained Q-factor is close to that obtained by calculations when κ_{Si} is 4×10^{-2}. It is important to note that in the calculation, the scattering loss is not considered and it is included in κ_{Si}. Therefore, $\kappa_{Si} = 4\times10^{-2}$ does not mean that the extinction coefficient of the a-Si used in this work is 4×10^{-2}. In order to obtain information on the scattering loss arising from structural imperfection, we measure the diffuse reflectance spectra. Figure 4(d) shows the total (diffuse + specular) reflectance spectrum measured using an integrating sphere for a large area (1×1 cm) sample with fixed spacer thickness (S = 650 nm, P = 750, D = 700, H = 100, T = 20 nm, and TD resonance wavelength = 1200 nm) under 8° incidence together with the specular reflectance under 5° incidence. The diffuse reflectance spectrum is obtained by subtracting the specular reflectance spectrum from the total reflectance one. The diffuse reflectance is ~0.17 at the resonance. Therefore, although a part of the reflectance dip is due to the scattering loss, it arises mainly from absorption. Later, we will estimate from the photocurrent spectra that κ_{Si} of the a-Si used in this work is of the order of 10^{-2}.

In Figure 4(a) and (b), the measured and calculated spectra show overall agreement. However, if we directly compare the measured and calculated reflectance spectra at a specific spacer thickness, there are small discrepancies, especially in the TD and MD resonance wavelengths (see Figure S7 in Supporting Information). In order to study the origin of the discrepancy, we

calculated the reflectance spectra for structures with slightly different parameters (Figure S7 in Supporting Information). We found that slight deviation of the structural parameters including the refractive index of Si strongly modifies the resonance wavelengths. Therefore, the discrepancy may arise from slight deviation of the fabricated structure from the designed one.

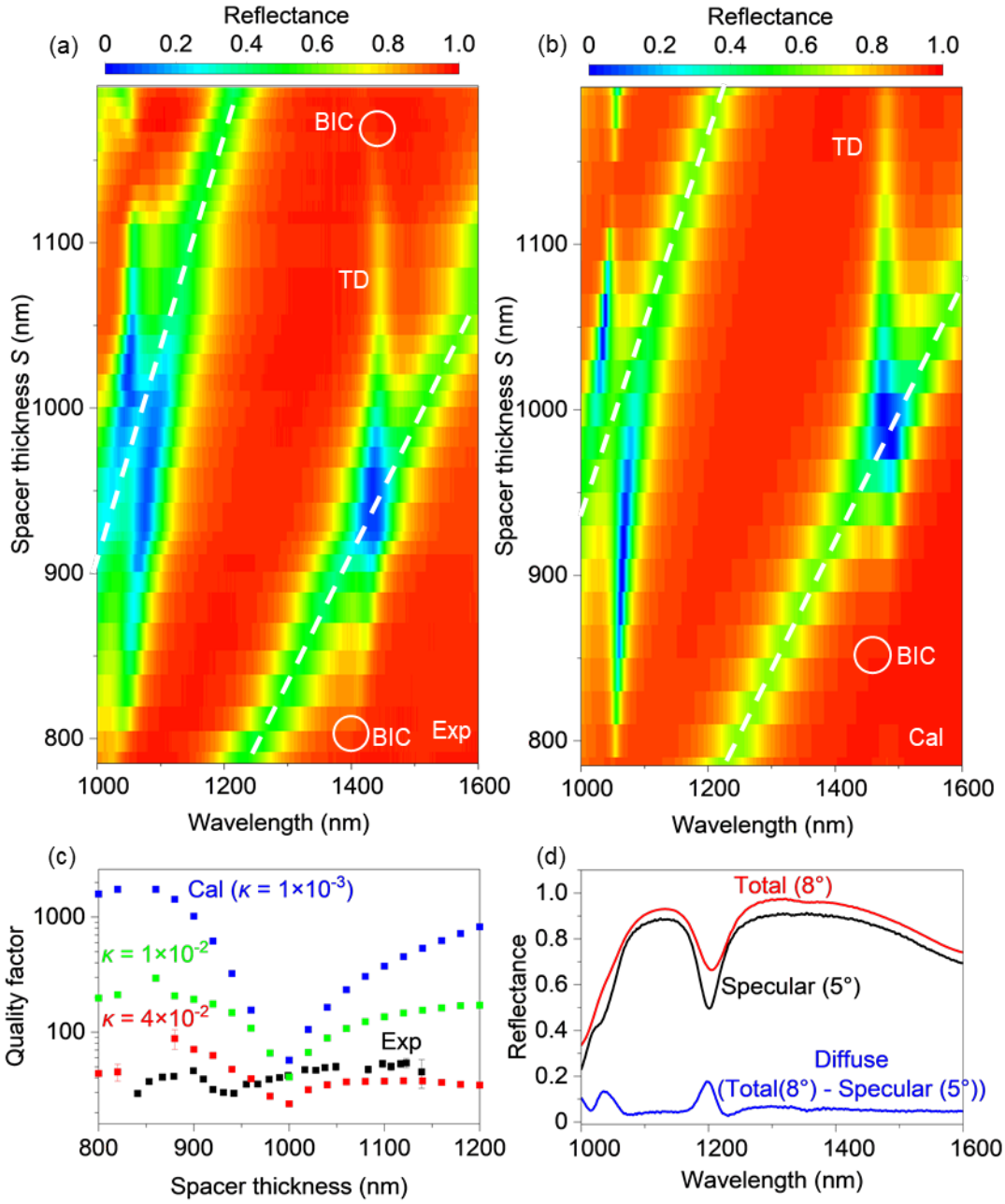


Figure 4. (a) Measured and (b) calculated reflectance spectra as a function of the spacer thickness. Other structural parameters are fixed (P = 750 nm, D = 700 nm, H = 100 nm, and T = 40 nm). A refractive index of 3.5+i4 × 10^{-2} is assumed for the calculation. White broken lines indicate the Fabry Pérot modes, and white circles designate the Fabry-Pérot BICs. (c) Q-factor of the TD resonance peak as a function of the spacer thickness. Q-factors obtained

from calculated reflectance spectra for $\boldsymbol{\kappa_{Si}} = 1\times10^{-3}$ (blue), 1×10^{-2} (green), and 4×10^{-2} (red) are also shown. (d) Reflectance spectra of a Si nanodisk array on a Au mirror structure. The structural parameters are P = 750, D = 700, H = 100, T = 20 nm, and S = 650 nm. (red) Total reflectance spectrum measured by using an integrating sphere with the incident angle of **8°**. (black) Specular reflectance spectrum measured with the incident angle of **5°**. (blue) Diffuse reflectance spectrum obtained by subtracting the specular reflectance from the total reflectance.

Figure 5(a-j) shows the photocurrent (responsivity) spectra (black) for different spacer thicknesses (S = 1162 nm - 849 nm) together with corresponding reflectance spectra (red). The reflectance dip around 1450 nm is due to the TD resonance. At the TD resonance, the photocurrent is enhanced, and the enhancement factor has a clear correlation with the depth of the reflectance dip. At S = 1162 nm (Figure 5(a)), the reflectance dip and the photocurrent peak almost disappear due to the Fabry-Pérot BIC. Reducing the spacer thickness from the BIC condition deepens the reflectance dip and increases the photocurrent. The photocurrent reaches the maximum at S = 995 nm. Further reducing the spacer thickness decreases the photocurrent. Therefore, the Si nanodisk hexagonal array on a mirror structure enhances the photocurrent in a narrow spectral range in the sub-bandgap wavelength range if the spacer thickness is tuned to satisfy the critical coupling condition. Note that slight broadening of the photocurrent spectra compared to the reflectance spectra is mainly due to the bandwidth (~20 nm) of the AOTF used to monochromatize white light from a supercontinuum laser.

In Figure 5, in addition to the photocurrent peak due to the TD resonance, that due to the Fabry-Pérot resonance appears. At S = 1027 nm (Figure 5(f)), the intensity is comparable to that of the TD resonance. As we discussed in Figure 2, absorption of Si by the Fabry-Pérot resonance has different κ_{Si} dependence from that of the TD resonance, and thus we can roughly estimate the value of κ_{Si} from the intensity ratio. We roughly estimate the extinction coefficient of the fabricated a-Si to be of the order of 10^{-2}. This value is similar to that estimated from the Q-factor of the reflectance dip in Figure 4(c).

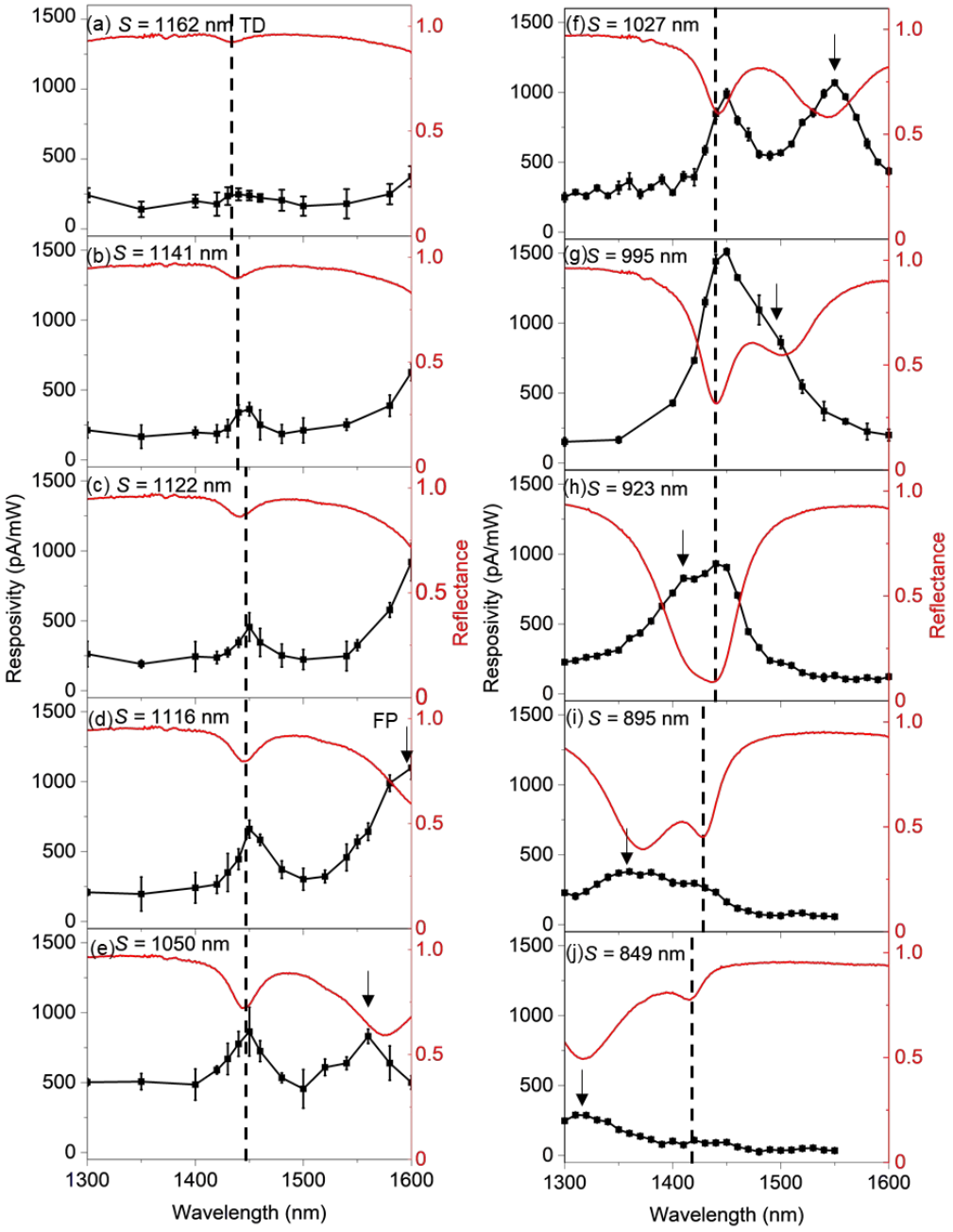


Figure 5. Photocurrent (responsivity) (black) and reflectance (red) spectra of a Si nanodisk array on a Au mirror structure with different spacer thicknesses (S = (a) 1162, (b) 1141, (c) 1122, (d) 1116, (e) 1050, (f) 1027, (g) 995, (h) 923, (i) 895, and (j) 849 nm). Other structural parameters are fixed (P = 750 nm, D = 700 nm, H = 100 nm, and T = 40 nm). The TD resonance wavelength is shown by a vertical dashed line. Arrows designate photocurrent peaks due to the Fabry Pérot resonance.

CONCLUSION

We proposed a Si nanodisk hexagonal array on a Au mirror structure as a platform for a Si-based narrow band photodetector operating in the sub-bandgap wavelength range. The structure possesses Fabry-Pérot BICs arising from the interference between the TD resonance of a nanodisk array and the mirror dipole. In the structure, the radiation loss can be precisely controlled by detuning the BIC condition by changing the spacer thickness, and thus the critical coupling condition can be achieved in a wide extinction coefficient range of the nanodisk array. We have studied the relation between the absorptance and the extinction coefficient, and found that, although a perfect absorption can be achieved even in a very small extinction coefficient range, e.g., ~10^{-4}, substantial amount of photons are absorbed by a Au mirror and do not contribute to the photocurrent in the small extinction coefficient range. Therefore, a relatively larger extinction coefficient, e.g., ~10^{-2}, is necessary to achieve over 90% absorptance in the Si nanodisk array. We produced the designed structure by a nanosphere lithography and studied the reflectance and photocurrent spectra as a function of the spacer thickness. We demonstrated that the photocurrent can be enhanced in the sub-bandgap wavelength range at the critical coupling condition, and the enhancement factor can be modulated by the spacer thickness.

Within this work, the responsivity value was not very large. This may be improved by properly engineering the band structure of the Si region in addition to the improvement of the device structure and the fabrication process. In particular, it is important to develop an amorphous Si layer having relatively large extinction coefficient in the sub-bandgap wavelength range and relatively long carrier lifetime. This has been achieved by engineering the band structure by Ar doping[11]. Application of the TD-based Fabry-Pérot BIC strategy to the defect-engineered amorphous Si may result in a high-responsivity narrow-band NIR photodetector.

Funding Sources

This work was partially supported by JSPS KAKENHI Grant Numbers 21H01748, 21H01782, 21K14496 and 22K18949

AUTHOR INFORMATION

Corresponding Author

Minoru Fujii

Department of Electrical and Electronic Engineering, Graduate School of Engineering, Kobe University, Rokkodai, Nada, Kobe 657-8501, Japan

E-mail:fujii@eedept.kobe-u.ac.jp

Hiroshi Sugimoto
Department of Electrical and Electronic Engineering, Graduate School of Engineering, Kobe University, Rokkodai, Nada, Kobe 657-8501, Japan
E-mail:sugimoto@eedept.kobe-u.ac.jp

Author Contributions

The manuscript was written through the contributions of all authors. All authors have given approval to final version of the manuscript.

AUTHOR DECLARATIONS

Conflict of Interest

The authors have no conflicts to disclose.

Supporting Information

The Supporting Information is available free of charge at https://pubs.acs.org/doi/.

Numerical simulation method; Temporal coupled mode theory (TCMT) for a Si nanodisk array on a mirror structure; Electric field distribution at the Fabry Pérot resonance; Absorptance spectra of a Si nanodisk array on a Bragg mirror structure; Absorptance of Si and Au at critical coupling conditions near the 1st and 2nd BICs; AFM image of a Si nanodisk array shown in Figure 3b; Schematic illustration of the fabricated device and photocurrent measurement; Effect of structural parameter deviation on reflectance spectra; Comparison between calculated and measured reflectance spectra; Electric field distribution at the magnetic dipole resonance (PDF)

References

(1) Kaushal, H.; Kaddoum, G. Optical Communication in Space: Challenges and Mitigation Techniques. *IEEE Commun. Surv. Tutorials* **2017**, *19* (1), 57–96. https://doi.org/10.1109/COMST.2016.2603518.

(2) Casalino, M.; Coppola, G.; De La Rue, R. M.; Logan, D. F. State-of-the-Art All-Silicon Sub-Bandgap Photodetectors at Telecom and Datacom Wavelengths. *Laser Photon. Rev.* **2016**, *10* (6), 895–921. https://doi.org/10.1002/lpor.201600065.

(3) Eng, P. C.; Song, S.; Ping, B. State-of-the-Art Photodetectors for Optoelectronic Integration at Telecommunication Wavelength. *Nanophotonics* **2015**, *4* (1), 277–302. https://doi.org/10.1515/nanoph-2015-0012.

(4) Li, W.; Valentine, J. Metamaterial Perfect Absorber Based Hot Electron Photodetection. *Nano Lett.* **2014**, *14* (6), 3510–3514. https://doi.org/10.1021/nl501090w.

(5) Casalino, M.; Sassi, U.; Goykhman, I.; Eiden, A.; Lidorikis, E.; Milana, S.; De Fazio, D.; Tomarchio, F.; Iodice, M.; Coppola, G.; Ferrari, A. C. Vertically Illuminated, Resonant Cavity Enhanced, Graphene–Silicon Schottky Photodetectors. *ACS Nano* **2017**, *11* (11), 10955–10963. https://doi.org/10.1021/acsnano.7b04792.

(6) Knight, M. W.; Sobhani, H.; Nordlander, P.; Halas, N. J. Photodetection with Active Optical Antennas. *Sci.* **2011**, *332* (6030), 702–704. https://doi.org/10.1126/science.1203056.

(7) Sobhani, A.; Knight, M. W.; Wang, Y.; Zheng, B.; King, N. S.; Brown, L. V.; Fang, Z.; Nordlander, P.; Halas, N. J. Narrowband Photodetection in the Near-Infrared with a Plasmon-Induced Hot Electron Device. *Nat. Commun.* **2013**, *4*, 1–6. https://doi.org/10.1038/ncomms2642.

(8) Clavero, C. Plasmon-Induced Hot-Electron Generation at Nanoparticle/Metal-Oxide Interfaces for Photovoltaic and Photocatalytic Devices. *Nat. Photonics* **2014**, *8* (2), 95–103. https://doi.org/10.1038/nphoton.2013.238.

(9) Geis, M. W.; Spector, S. J.; Grein, M. E.; Schulein, R. T.; Yoon, J. U.; Lennon, D. M.; Deneault, S.; Gan, F.; Kaertner, F. X.; Lyszczarz, T. M. CMOS-Compatible All-Si High-Speed Waveguide Photodiodes with High Responsivity in near-Infrared Communication Band. *IEEE Photonics Technol. Lett.* **2007**, *19* (3), 152–154. https://doi.org/10.1109/LPT.2006.890109.

(10) Doylend, J. K.; Jessop, P. E.; Knights, A. P. Silicon Photonic Resonator-Enhanced Defect-Mediated Photodiode for Sub-Bandgap Detection. *Opt. Express* **2010**, *18* (14), 14671. https://doi.org/10.1364/OE.18.014671.

(11) Zhao, J. H.; Li, C. H.; Li, X. Bin; Chen, Q. D.; Chen, Z. G.; Sun, H. B. NIR Photodetector Based on Nanosecond Laser-Modified Silicon. *IEEE Trans. Electron Devices* **2018**, *65* (11), 4905–4909. https://doi.org/10.1109/TED.2018.2869912.

(12) Chen, N. K.; Gao, Y. C.; Zhao, J. H.; Li, C. H.; Chen, Q. D.; Sun, H. B.; Zhang, S.; Li, X. Bin. Inert Gas Element as Active Infrared-Absorption Source and Donor in Silicon

for Forbidden-Wavelength Sensing. *Adv. Opt. Mater.* **2024**, *12* (20), 1–8. https://doi.org/10.1002/adom.202400361.

(13) Jackson, W. B.; Johnson, N. M.; Biegelsen, D. K. Density of Gap States of Silicon Grain Boundaries Determined by Optical Absorption. *Appl. Phys. Lett.* **1983**, *43* (2), 195–197. https://doi.org/10.1063/1.94278.

(14) Reiter, S.; Koper, N.; Reineke-Koch, R.; Larionova, Y.; Turcu, M.; Krügener, J.; Tetzlaff, D.; Wietler, T.; Höhne, U.; Kähler, J. D.; Brendel, R.; Peibst, R. Parasitic Absorption in Polycrystalline Si-Layers for Carrier-Selective Front Junctions. *Energy Procedia* **2016**, *92* (92), 199–204. https://doi.org/10.1016/j.egypro.2016.07.057.

(15) Li, C.; Zhao, J. H.; Chen, X.; Li, F. Y.; Zhang, X. L.; Chen, Z. G.; Chen, Q. D. Investigation of the Structure and Optical Absorption of Silicon Coated with a Chromium Film after Femtosecond Laser Irradiation. *Semicond. Sci. Technol.* **2020**, *35* (1). https://doi.org/10.1088/1361-6641/ab57eb.

(16) Tull, B. R.; Winkler, M. T.; Mazur, E. The Role of Diffusion in Broadband Infrared Absorption in Chalcogen-Doped Silicon. *Appl. Phys. A Mater. Sci. Process.* **2009**, *96* (2), 327–334. https://doi.org/10.1007/s00339-009-5200-8.

(17) Logan, D. F.; Knights, A. P.; Jessop, P. E.; Tarr, N. G. Defect-Enhanced Photo-Detection at 1550 Nm in a Silicon Waveguide Formed via LOCOS. *Semicond. Sci. Technol.* **2011**, *26* (4), 045009. https://doi.org/10.1088/0268-1242/26/4/045009.

(18) Bradley, J. D. B.; Jessop, P. E.; Knights, A. P. Silicon Waveguide-Integrated Optical Power Monitor with Enhanced Sensitivity at 1550nm. *Appl. Phys. Lett.* **2005**, *86* (24), 241103. https://doi.org/10.1063/1.1947379.

(19) Garín, M.; Fenollosa, R.; Alcubilla, R.; Shi, L.; Marsal, L. F.; Meseguer, F. All-Silicon Spherical-Mie-Resonator Photodiode with Spectral Response in the Infrared Region. *Nat. Commun.* **2014**, *5* (1), 3440. https://doi.org/10.1038/ncomms4440.

(20) Hasebe, H.; Moriasa, K.; Yamashita, K.; Sugimoto, H.; Fujii, M. Toroidal Dipole-Induced Photocurrent Enhancement in Si Nanodisk Hexagonal Array below the Band Gap. *ACS Photonics* **2022**, *9* (10), 3302–3309. https://doi.org/10.1021/acsphotonics.2c00660.

(21) Moriasa, K.; Hasebe, H.; Sugimoto, H.; Fujii, M. Bound States in the Continuum (BIC) in Silicon Nanodisk Array on Mirror Structure: Perfect Absorption Associated with Quasi-BIC below the Bandgap. *J. Appl. Phys.* **2023**, *133* (17). https://doi.org/10.1063/5.0146896.

(22) Miroshnichenko, A. E.; Evlyukhin, A. B.; Yu, Y. F.; Bakker, R. M.; Chipouline, A.; Kuznetsov, A. I.; Luk'yanchuk, B.; Chichkov, B. N.; Kivshar, Y. S. Nonradiating Anapole Modes in Dielectric Nanoparticles. *Nat. Commun.* **2015**, *6* (1), 8069. https://doi.org/10.1038/ncomms9069.

(23) Hasebe, H.; Sugimoto, H.; Hinamoto, T.; Fujii, M. Coupled Toroidal Dipole Modes in Silicon Nanodisk Metasurface: Polarization Independent Narrow Band Absorption and Directional Emission. *Adv. Opt. Mater.* **2020**, *8* (22), 2001148. https://doi.org/10.1002/adom.202001148.

(24) Piper, J. R.; Liu, V.; Fan, S. Total Absorption by Degenerate Critical Coupling. *Appl. Phys. Lett.* **2014**, *104* (25), 251110. https://doi.org/10.1063/1.4885517.

(25) Suh, W.; Member, S.; Wang, Z.; Fan, S.; Wonjoo Suh; Zheng Wang; Shanhui Fan. Temporal Coupled-Mode Theory and the Presence of Non-Orthogonal Modes. *IEEE J. Quantum Electron.* **2004**, *40* (10), 1511–1518.

(26) Verslegers, L.; Yu, Z.; Catrysse, P. B.; Fan, S. Temporal Coupled-Mode Theory for Resonant Apertures. *J. Opt. Soc. Am. B* **2010**, *27* (10), 1947. https://doi.org/10.1364/JOSAB.27.001947.

(27) Manolatou, C.; Khan, M. J.; Fan, S.; Villeneuve, P. R.; Haus, H. A.; Joannopoulos, J. D. Coupling of Modes Analysis of Resonant Channel Add-Drop Filters. *IEEE J. Quantum Electron.* **1999**, *35* (9), 1322–1331. https://doi.org/10.1109/3.784592.

(28) Xu, L.; Rahmani, M.; Zangeneh Kamali, K.; Lamprianidis, A.; Ghirardini, L.; Sautter, J.; Camacho-Morales, R.; Chen, H.; Parry, M.; Staude, I.; Zhang, G.; Neshev, D.; Miroshnichenko, A. E. Boosting Third-Harmonic Generation by a Mirror-Enhanced Anapole Resonator. *Light Sci. Appl.* **2018**, *7* (1), 44. https://doi.org/10.1038/s41377-018-0051-8.

(29) Yang, G.; Dev, S. U.; Allen, M. S.; Allen, J. W.; Harutyunyan, H. Optical Bound States in the Continuum Enabled by Magnetic Resonances Coupled to a Mirror. *Nano Lett.* **2022**, *22* (5), 2001–2008. https://doi.org/10.1021/acs.nanolett.1c04764.

(30) Jin, R.; Huang, L.; Zhou, C.; Guo, J.; Fu, Z.; Chen, J.; Wang, J.; Li, X.; Yu, F.; Chen, J.; Zhao, Z.; Chen, X.; Lu, W.; Li, G. Toroidal Dipole BIC-Driven Highly Robust Perfect Absorption with a Graphene-Loaded Metasurface. *Nano Lett.* **2023**, *23* (19), 9105–9113. https://doi.org/10.1021/acs.nanolett.3c02958.

(31) Zhou, C.; Huang, L.; Jin, R.; Xu, L.; Li, G.; Rahmani, M.; Chen, X.; Lu, W.; Miroshnichenko, A. E. Bound States in the Continuum in Asymmetric Dielectric

Metasurfaces. *Laser Photonics Rev.* **2023**, *17* (3), 1–8. https://doi.org/10.1002/lpor.202200564.

(32) Sun, X.; Sun, J.; Wang, Z.; Wang, L.; Qiu, F.; Wen, L. Manipulating Dual Bound States in the Continuum for Efficient Spatial Light Modulator. *Nano Lett.* **2022**, *22* (24), 9982–9989. https://doi.org/10.1021/acs.nanolett.2c03539.

(33) Wu, F.; Fan, C.; Zhu, K.; Wu, J.; Qi, X.; Sun, Y.; Xiao, S.; Jiang, H.; Chen, H. Tailoring Electromagnetic Responses in a Coupled-Grating System with Combined Modulation of near-Field and Far-Field Couplings. *Phys. Rev. B* **2022**, *105* (24), 245417. https://doi.org/10.1103/PhysRevB.105.245417.

(34) Hsu, C. W.; Zhen, B.; Stone, A. D.; Joannopoulos, J. D.; Soljačić, M. Bound States in the Continuum. *Nat. Rev. Mater.* **2016**, *1* (9), 16048. https://doi.org/10.1038/natrevmats.2016.48.

(35) Jackson, W. B.; Amer, N. M. Direct Measurement of Gap-State Absorption in Hydrogenated Amorphous Silicon by Photothermal Deflection Spectroscopy. *Phys. Rev. B* **1982**, *25* (8), 5559–5562. https://doi.org/10.1103/PhysRevB.25.5559.

(36) Fan, H. Y.; Ramdas, A. K. Infrared Absorption and Photoconductivity in Irradiated Silicon. *J. Appl. Phys.* **1959**, *30* (8), 1127–1134. https://doi.org/10.1063/1.1735282.

(37) Spear, W. .; Loveland, R. .; A.Al-Sharbaty. The Temperature Dependence f Photoconductivity in A-Si. *J. Non. Cryst. Solids* **1974**, *15* (3), 410–422. https://doi.org/10.1016/0022-3093(74)90147-1.

(38) Brodsky, M. H.; Title, R. S.; Weiser, K.; Pettit, G. D. Structural, Optical, and Electrical Properties of Amorphous Silicon Films. *Phys. Rev. B* **1970**, *1* (6), 2632–2641. https://doi.org/10.1103/PhysRevB.1.2632.

(39) Okutani, T.; Shikata, M.; Ichimura, S.; Shimizu, R. Angular Distribution of Si Atoms Sputtered by KeV Ar+ Ions. *J. Appl. Phys.* **1980**, *51* (5), 2884–2887. https://doi.org/10.1063/1.327957.

For Table of Contens Use Only

Title : Sub-bandgap Photocurrent Enhancement in Silicon Nanodisk Hexagonal Array Induced by Fabry-Pérot Bound States in the Continuum

Authors : Keisuke Moriasa, Hiroaki Hasebe, Hiroshi Sugimoto*, and Minoru Fujii*

Synopsis : A hexagonal array of a silicon nanodisk on mirror for narrowband photocurrent enhancement induced by Fabry-Pérot bound states in the continuum in the sub-bandgap wavelength regime.

